



AFRL-AFOSR-JP-TR-2018-0063

Multi-functional Infrared Sensor

Sang Jun Lee
KOREA RESEARCH INSTITUTE OF STANDARDS AND SCIENCE (KRISS)
1 DORYONG DONG YUSEONG GU
DAEJUN-CITY, 305-340
KR

08/22/2018
Final Report

DISTRIBUTION A: Distribution approved for public release.

Air Force Research Laboratory
Air Force Office of Scientific Research
Asian Office of Aerospace Research and Development
Unit 45002, APO AP 96338-5002

REPORT DOCUMENTATION PAGE				<i>Form Approved</i> OMB No. 0704-0188	
<p>The public reporting burden for this collection of information is estimated to average 1 hour per response, including the time for reviewing instructions, searching existing data sources, gathering and maintaining the data needed, and completing and reviewing the collection of information. Send comments regarding this burden estimate or any other aspect of this collection of information, including suggestions for reducing the burden, to Department of Defense, Executive Services, Directorate (0704-0188). Respondents should be aware that notwithstanding any other provision of law, no person shall be subject to any penalty for failing to comply with a collection of information if it does not display a currently valid OMB control number.</p> <p>PLEASE DO NOT RETURN YOUR FORM TO THE ABOVE ORGANIZATION.</p>					
1. REPORT DATE (DD-MM-YYYY) 22-08-2018		2. REPORT TYPE Final		3. DATES COVERED (From - To) 30 Sep 2014 to 29 Mar 2018	
4. TITLE AND SUBTITLE Multi-functional Infrared Sensor				5a. CONTRACT NUMBER	
				5b. GRANT NUMBER FA2386-14-1-4094	
				5c. PROGRAM ELEMENT NUMBER 61102F	
6. AUTHOR(S) Sang Jun Lee				5d. PROJECT NUMBER	
				5e. TASK NUMBER	
				5f. WORK UNIT NUMBER	
7. PERFORMING ORGANIZATION NAME(S) AND ADDRESS(ES) KOREA RESEARCH INSTITUTE OF STANDARDS AND SCIENCE (KRISS) 1 DORYONG DONG YUSEONG GU DAEJUN-CITY, 305-340 KR				8. PERFORMING ORGANIZATION REPORT NUMBER	
9. SPONSORING/MONITORING AGENCY NAME(S) AND ADDRESS(ES) AOARD UNIT 45002 APO AP 96338-5002				10. SPONSOR/MONITOR'S ACRONYM(S) AFRL/AFOSR IOA	
				11. SPONSOR/MONITOR'S REPORT NUMBER(S) AFRL-AFOSR-JP-TR-2018-0063	
12. DISTRIBUTION/AVAILABILITY STATEMENT A DISTRIBUTION UNLIMITED: PB Public Release					
13. SUPPLEMENTARY NOTES					
14. ABSTRACT Final report was received in June 2018 but due to SF425 and dd0882 was missing and received late time, it was dated late July					
15. SUBJECT TERMS Microwave Infrared, Plasmonics, Quantum Dot Detector, AOARD					
16. SECURITY CLASSIFICATION OF:			17. LIMITATION OF ABSTRACT	18. NUMBER OF PAGES	19a. NAME OF RESPONSIBLE PERSON
a. REPORT	b. ABSTRACT	c. THIS PAGE			KIM, TONY
Unclassified	Unclassified	Unclassified	SAR		19b. TELEPHONE NUMBER (include area code) 315-227-7008

GRANT NO.: FA2386-14-1-4094

PROJECT TITLE: Multi-functional Infrared Sensor

PERIOD OF PERFORMANCE: Sep, 30 2017 to Mar, 29 2018

PRINCIPAL INVESTIGATOR:

Dr. Sang Jun Lee, Principal Research Scientist

Korea Research Institute Standards and Science

Address: 267 Gajeong-ro, Yuseong-gu, Daejeon 305-600, Korea

Email: sjlee@kriss.re.kr, Phone: +82 42 868 5127, Fax: +82 42 868 5047

I. Accomplishments This Period

Paper

Final performance report: No Cost Extension

1. Khagendra Bhattarai, Sinhara Silva, Kun Song, Augustine Urbas, Sang Jun Lee, Zahyun Ku, and Jiangfeng Zhou, "Metamaterial Perfect Absorber Analyzed by a Meta-cavity Model Consisting of Multilayer Metasurfaces," arXiv:1705.02681 (2017).
2. Jun Oh Kim, Tien Dai Nguyen, Zahyun Ku, Augustine Urbas, Sang-Woo Kang, and Sang Jun Lee, "Short wavelength infrared photodetector and light emitting diode based on InGaAsSb," *Proceedings of the SPIE* 10177, 101772M1-6 (2017).
3. (Invited Paper) Khagendra Bhattarai, Sinhara R. Silva, Augustine Urbas, Sang Jun Lee, Zahyun Ku, and Jiangfeng Zhou, "Angle-Dependent Spoof Surface Plasmons in Metallic Hole Arrays at Terahertz Frequencies," *IEEE Journal of Selected Topics in Quantum Electronics* 23(4), (2017).
4. Khagendra Bhattarai, Sinhara Silva, Kun Song, Augustine Urbas, Sang Jun Lee*, Zahyun Ku, and Jiangfeng Zhou, "Metamaterial Perfect Absorber Analyzed by a Meta-cavity Model Consisting of Multilayer Metasurfaces," *Sci. Rep.* 7: 10569 | DOI:10.1038/s41598-017-10520-w (2017).

Conference (abstract, talk, poster)

1. Jiyeon Jeon, Deok-Kee Kim, Jun Oh Kim, Won Chegal, Jiangfeng Zhou, Augustine Urbas, Zahyun Ku, and Sang Jun Lee, "Adaptive multispectral detection using IR transmission spectra through quasi-3D circular coaxial aperture array," The 19th International Symposium on the Physics of Semiconductors and Applications, ISPSA (2018).
2. Jehwan Hwang, Boram Oh, Eun Kyu Kim, Yeongho Kim, Jun Oh Kim, Won Chegal, Sang-Woo Kang, David Czaplowski, Jong Eun Ryu, Jiangfeng Zhou, Augustine Urbas, Zahyun Ku, and Sang Jun Lee, "Experimental verification of high-performance linear polarizer using stacked 1D subwavelength gratings," The 19th International Symposium on the Physics of Semiconductors and Applications, ISPSA (2018).
3. Jehwan Hwang, Daehyeon Ku, Jun Oh Kim, Eun Kyu Kim, Augustine Urbas, Zahyun Ku, and Sang Jun Lee, "1D subwavelength gratings-dielectric-T2SL detector: Highly improved performance of MWIR polarization detection," The 8th International Conference on Metamaterials, Photonic Crystals and Plasmonics, META 2017 (2017).

4. J. Jeon, K. Bhattarai, D.-K. Kim, J. O. Kim, J. Zhou, A. Urbas, Z. Ku and S. J. Lee, "Surface Plasmonic - Cavity System," The 8th International Conference on Metamaterials, Photonic Crystals and Plasmonics, META 2017 (2017).
5. B. Oh, X. E. Huang, D.-K. Kim, J. O. Kim, S. J. Lee, A. Urbas, Z. Ku, D. A. Czaplewski, I. W. Jung, and J. E. Ryu, "Nanoimprint-lithographically fabricated stacked 1D gratings for improved MWIR polarization detection," The 8th International Conference on Metamaterials, Photonic Crystals and Plasmonics, META 2017 (2017).
6. Junoh Kim, Tien Dai Nguyen, Zahyun Ku, Augustine Urbas, Sang-Woo Kang, and Sang Jun Lee, "Short wavelength infrared photodetector and light emitting diode based on InGaAsSb," SPIE Defense + Security (2017).

II. Technical Progress during Period

A. Responsivity enhancement of quantum dot-in-a-well infrared photodetectors using plasmonic structures

A wide range of applications, including those of medical and military interest, has fueled research in infrared (IR) photodetectors. Mercury-cadmium-telluride detectors (MCTs) are the standard to date, but are often prohibitively expensive and operate optimally at lower temperature (as compared with quantum dots based detector). Quantum dot-in-a-well (DWELL) detectors have emerged as potential competitors to MCTs by combining the advantages of quantum dot detector (normal-incidence detection, high photoelectric gain, potential for low dark currents, and high-temperature operation), with those of quantum well detector (better sensitivity and control over operating wavelength), and are approaching MCTs in terms of responsivity and specific-detectivity (although DWELL detectors still exhibit worse performance than MCTs).

DWELL detector performance can be enhanced by surface plasmon polariton (SPP) excitation caused by the inclusion of sub-wavelength metallic hole arrays (MHAs). SPPs are the collective oscillations of electron plasma in the metallic structure, e.g. MHA, excited by electromagnetic (EM) radiation, which can concentrate light into subwavelength scale beyond the diffraction limit and thereby significantly enhancing the EM field. Localized surface plasmon (LSP) confines surface plasmon in the vicinity of subwavelength resonators, e.g. metallic disks, which also can significantly enhance the EM field near the surface of the resonators, and thereby improving the performance of the photodetectors. By means of computer simulation, we investigate the integration of different plasmonic architectures with DWELL detectors to enable further enhancement and make comparisons between plasmonic structures. Nine variations of the DWELL IR photodetector are investigated. Three of these are base designs: the front-side illuminated IR detector (FSD), the back-side illuminated IR detector (BSD), and the back-side illuminated IR detector with a gold (Au) ground plane (BSD:AGP). The other six are created by integrating either a gold disk-array (ADA) or a gold hole-array (AHA) onto each of the three base designs. These structure combinations are abbreviated as FSD:ADA, BSD:AHA, BSD:AGP:ADA, etc. The DWELL detector and ADA/AGP/AHA structures could be manufactured using nanofabrication techniques.

A finite integration technique based 3D full field simulations performed in *CST Microwave Studio* was used to evaluate the performance of each configuration. A single element DWELL device (Figure 1) is analyzed with an incident TEM wave produced by using appropriate perfect electric/magnetic boundary conditions. The spectral responsivity $R(\lambda)$ of DWELL device can be calculated using Equation (1), where the internal quantum efficiency η_{IQE} is assumed to be 1, $N_0(\lambda)$ is the incident photon flux, $P_{BB}(\lambda, T)$ is the power radiated by a blackbody of a given temperature per unit area per unit wavelength (determined from Planck's law), and A_{EA} is the power absorbed in the active layer as determined by Equation (2). Equation (2) is derived by assuming a complex dielectric constant in Poynting's theorem and considering only dielectric loss. Losses in the contact layers can be calculated analogously, but only the active layer contributes to the responsivity. Stronger effect to create photo-induced current in detector for an electric field component perpendicular to the surface is accounted for by the parameter, ξ , which is estimated to be ~ 8 . However, the perpendicular component, E_z , will not exist without the excitations of SPP or LSP for normally incident light.

$$R(\lambda) = \left(\frac{\eta_{IQE} \cdot N_0(\lambda) \cdot e^-}{P_{BB}(\lambda, T)} \right) \cdot A_{EA} \quad (1)$$

$$A_{EA} = \int \frac{\omega \epsilon''_{EA}(\lambda) \cdot \left[|E_{EA}^x(\lambda)|^2 + \xi |E_{EA}^z(\lambda)|^2 \right]}{2} dV_{EA} \quad (2)$$

The Drude model is applied to the gold plasmonic structures and ground plane (when present), where a fitting parameter γ is introduced to account for the increase in collision frequency in thin gold film as compared to that determined for the bulk material, such that $\omega_{c, film} = \gamma \cdot \omega_{c, bulk}$. In general, γ is unknown but larger than 1 ($\gamma = 1.4$ was found to fit the experimental values for IR region and was used here). The responsivity of the detector could be improved by smooth plasmonic surface (low γ) obtained at a very low deposition rate. The responsivities for the hole and disk arrays have been optimized with respect to their period p and diameter d . Lastly, the responsivity dependence on the plasmonic layer thickness t_{Au} is examined. The performance of the plasmonic structures will be compared by defining the enhancement for a given base detector (FSD, BSD or BSD:AGP) as the ratio of the responsivity with a given plasmonic structure to the responsivity without it. This will allow determination of the best plasmonic structure to be used for given parameters.

The design and composition of the FSD is displayed in Figure 1(a) and 1(b). The FSD is designed to detect photons in the 4 -12 μm range, with peaks located near 6.5 and 10 μm . Note that the 10 μm peak resides in the long-wave infrared atmospheric window. This spectral response was measured using a Fourier transform infrared spectrometer (Figure 1(c)), which was used for our simulation to calculate the imaginary part of the refractive index for effective active layer ($k = \eta_{QE} \cdot R_s$, where η_{QE} is the measured quantum

efficiency (\sim external quantum efficiency) and R_s is obtained by normalizing the measured spectral response between 0 and 1). Figure 1(e) shows that the calculation of the absorption in each layer of the FSD by Equation (2) and indicates that most of the absorption occurs in the active layer at $\sim 6.5 \mu\text{m}$ and in the bottom contact layer at $\sim 10 \mu\text{m}$. Multiplying the absorption in the active layer by the responsivity (when using the photodetector with 100% absorption and illuminated by blackbody at 900K in the 4 -12 μm range) in the parenthesis as shown in Equation (1) yields the simulated detector responsivity as shown in Figure 1(f), which is in excellent agreement with the experimental results as shown in the inset.

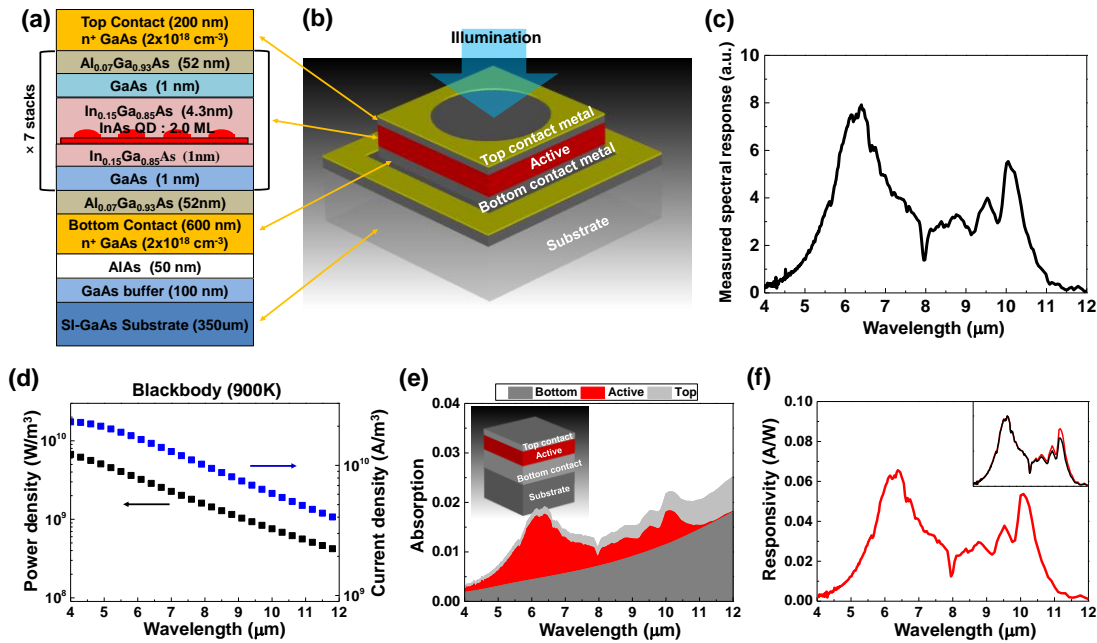


Figure 1. (a) Composition of DWELL detector layers. (b) Schematic of an FSD cell. The hole in the top is an aperture for the entry of photons and is distinct from gold hole-array plasmonic structures. (c) Experimental data for the reponsivity of the FSD expressed in arbitrary units. (d) Power density spectrum and spectral current density radiating from the blackbody at 900K. Spectral current density is the theoretical amount of free charge that could be generated at a given wavelength per unit of detector area if the internal quantum efficiency is 1. (e) Power absorbed in each layer of FSD. Substrate loss is negligible. (f) Simulated spectral responsivity of the FSD. Comparison with experimental data is shown in the inset.

Figure 2 indicates the simulated responsivities of the BSD and BSD:AGP designs. In the actual detector devices, e.g. focal plan array (FPA), the AGP serves as the contact connected to the read-out circuit (ROIC) via indium bumps. Like with the FSD, most of the absorption occurs in the active layer. For the main absorption peaks of the active layers at 6.25 μm wavelength (Figure 2(d) and 2(g)), the design with AGP increases the absorption by a factor of 5 (from ~ 0.01 to ~ 0.05). Correspondingly, the responsivity (Figure

2(e) and 2(h)) increases by ~ 5 (~ 0.06 A/W to ~ 0.29 A/W). As indicated by the responsivity, the BSD:AGP configuration has the best detector performance and is used as a basis of comparison for the other designs.

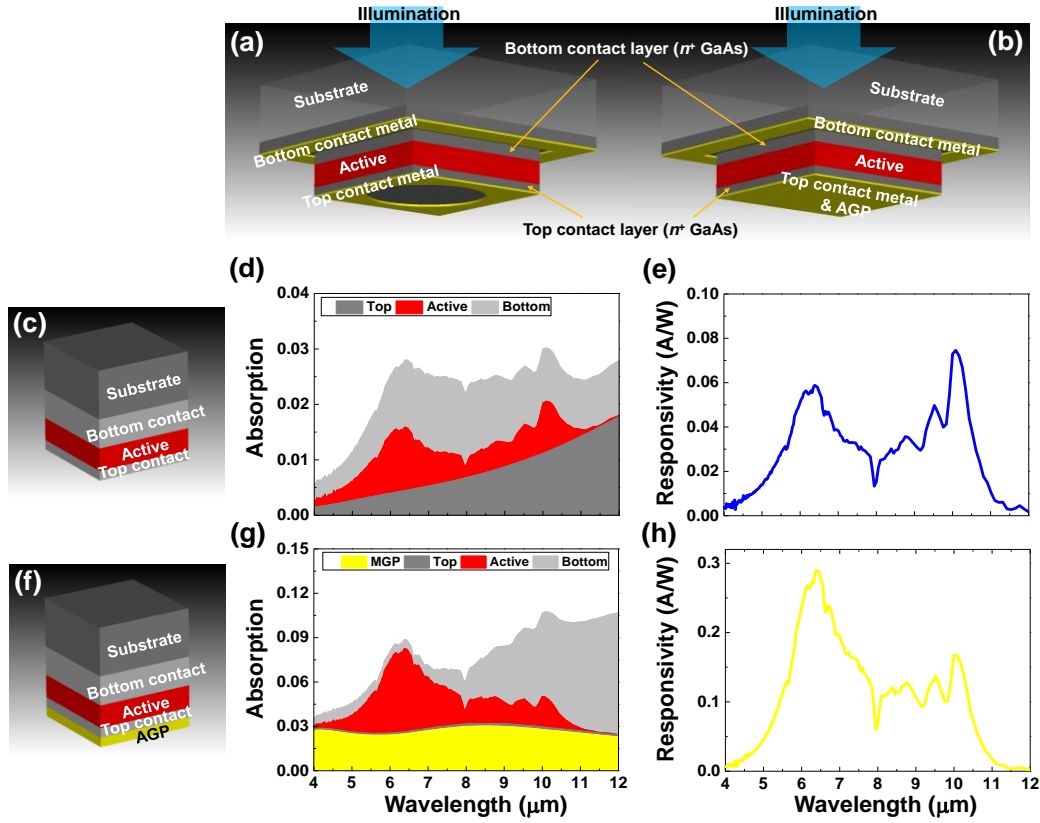


Figure 2. (a) Profiles of physical BSD and (b) BSD:AGP designs. Simplified versions used for simulation are shown in (c) and (f) with their corresponding absorptions (d),(g) and responsivities (e),(h).

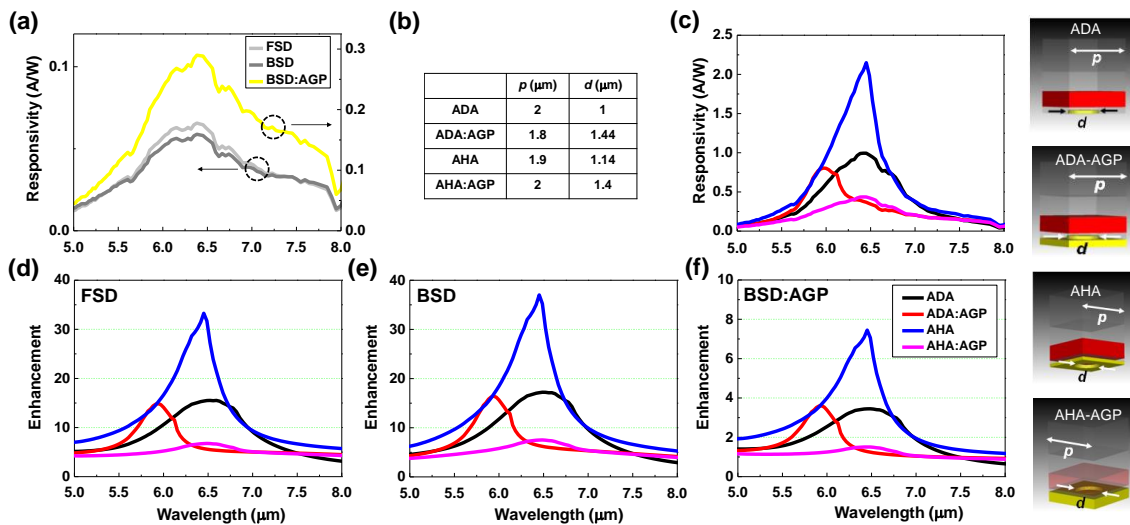


Figure 3. (a) Comparison of responsivities for the FSD, BSD (left-hand scale), and BSD:AGP (right-hand scale) designs. (b) Optimal period, p , and diameter, d , for the plasmonic structures. (c) Responsivity of the four type of plasmonic structures: ADA, ADA:AGP, AHA, AHA:AGP as shown in schematics on the right-side. (d)-(f) Enhancement of four configurations with respect to FSD, BSD and BSD:AGP, respectively.

The Au ground plane thickness is $0.2 \mu\text{m}$ and the plasmonic structure layer thickness is $0.1 \mu\text{m}$ for all plots. In the following, we study the improvement of device performance due to SPP and LSP. We choose two widely used plasmonic structures, ADA and AHA, to excite the LSP and SPP, respectively. To integrate these plasmonic structures into actual devices, e.g. FPA, we also considered structures with AGP. Four BSD structures (ADA, ADA:AGP, AHA and AHA:AGP) are schematically shown in Figure 3, where AHA and ADA are embedded into the top contact layer. In the case of AGP designs, the array structures (ADA and AHA) are placed in contact with the AGP. We replot the responsivity for FSD, BSD and BSD:AGP in Figure 2(a) and use them as references in Figure 3(d)-3(f) to compare the enhancement due to four plasmonic structures. The optimum values for the diameter and period of the arrays of plasmonic structures are tabulated in Figure 3b and responsivities using those parameters for the corresponding structures are plotted in Figure 3(c). The AHA design exhibits highest responsivity with peak value of 2.2 A/W in comparison to ADA design with peak value of 1.0 A/W . We attribute the better performance of AHA to strong electric field E_z of SPP which extended more into the active layer compared to that of LSP in ADA. With the AGP directly attached to AHA and ADA, the responsivities are decreased, especially for AHA. Enhancement factors for each base detector type are plotted in Figure 3(d)-3(f), where we found both AHA and ADA effectively improves the performance for all three types of devices, however, the enhancement resulting from AHA decreases significantly when AGP is added.

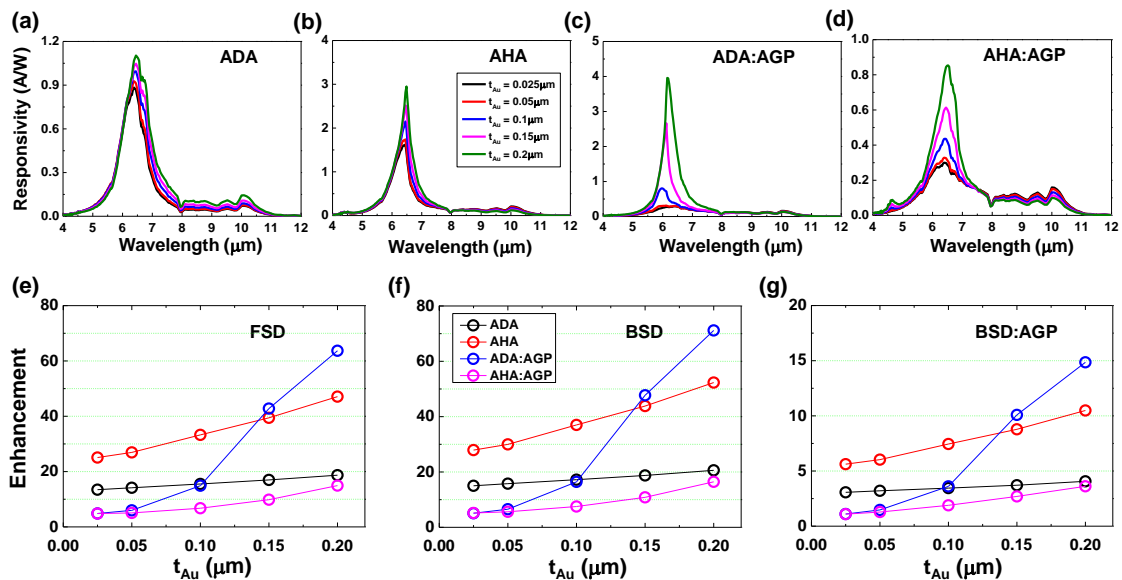


Figure 4. (a)-(d) Responsivities for each plasmonic structure type on as the thickness, t_{Au} , of the plasmonic structure layer is adjusted. (e)-(g) Corresponding enhancements of four configurations (ADA, AHA, ADA:AGP, AHA:AGP) using BSD, FSD and BSD:AGP base devices as references, respectively.

To improve the performance of AGP designs, we increase the thickness of plasmonic structures. As shown in Figure 4(a) and 4(b), when the thickness increases, the responsivity for AHA and ADA increases by minor amount. However, responsivity for the ADA:AGP design increases significantly (Figure 4(c)). For $t_{Au} = 0.2 \mu\text{m}$, at the peak wavelength of $6.19 \mu\text{m}$, the responsivity of ADA:AGP reaches 3.95 A/W , which is higher than peak values of ADA (1.10 A/W) and AHA (2.95 A/W) designs. The trend of increasing responsivity for ADA:AHA indicates stronger LSP resonance when t_{Au} increases. In particular, the most notable change occurs when t_{Au} increases from $0.1 \mu\text{m}$ to $0.15 \mu\text{m}$, where the responsivity increases from 0.80 A/W to 2.67 A/W , indicating that LSP resonance requires enough thickness ($> 0.1 \mu\text{m}$) of metal to establish when ADA is attached to AGP. Figure 4(d) shows that the improvement of responsivity of AHA:AGP design as t_{Au} increases are very limited, which results from strong damping of SPP by AGP due to the long-range surface wave nature. As indicated in Figure 4(e) to 4(g), the enhancements of all four designs as function of t_{Au} increases as t_{Au} increases, which is in consistent with the trend of responsivity shown in Figure 4(a) to 4(d). Among all designs, the ADA:AGP shows the most dramatic increase from the lowest at $t_{Au} = 0.025 \mu\text{m}$ to the best at $t_{Au} = 0.2 \mu\text{m}$. Of the three base detector designs, the BSD:AGP has superior performance and is most commonly used for applications (IR imagery), and thus is the most important. The BSD:AGP responsivity is dramatically enhanced by nearly a factor of 8 with the inclusion of a $0.1 \mu\text{m}$ thick layer of AHA structures. If a thicker layer is acceptable, then the enhancement can improve to a factor of 15 at $0.2 \mu\text{m}$ by using the ADA:AGP configuration instead. Although the enhancement factor is greater for the FSD and BSD designs, their overall performance is still inferior to the BSD:AGP. The enhancement factors for the FSD and BSD detectors compare favorably with experimental data presented by other references, suggesting that the simulated results for the BSD:AGP are also of good quality.

B. Fabry-Perot cavity resonance enabling highly polarization-sensitive double-layer gold grating

Infrared (IR) polarimetric imaging has attracted much attention due to various applications such as remote sensing, military surveillance and industrial monitoring. However, a single layer of 1-dimensional (1D) grating to be conventionally integrated with IR focal plane array device intrinsically has the limited extinction ratio (defined as the ratio of TM transmission to TE transmission) and TM transmission efficiency due to the large impedance mismatch between incoming medium and 1D metal grating. Here, we investigated experimentally and theoretically new design, stacked 1D subwavelength

gratings, with a superior linear polarization extinction, which is based on the Fabry-Perot (FP) cavity formed by two layers of 1D subwavelength grating and operates in the mid-wave IR range. The structure of stacked 1D gratings consists of two identical metal gratings, separated by a dielectric film (spacer) as shown in Figure 5(a). The thickness of the spacer layer, $t_{BCB} = 0.25 \mu\text{m}$ was determined in consideration of the linear polarization performance using a multiple-layer model and a finite integration technique based simulation as shown in Figure 5(b) and 5(c). TM transmission efficiency of stacked 1D gratings is improved as compared with a single 1D grating, which results from the FP cavity resonance between two 1D grating layers, where FP phase condition (γ) at $\lambda = 4.2 \mu\text{m}$ is found to be -2π as indicated in Figure 5(c). As a result, the polarization performance of a single 1D grating and stacked 1D gratings was characterized by means of InAs/GaSb type-II superlattice (T2SL) based MWIR camera as displayed in Figure 5(d).

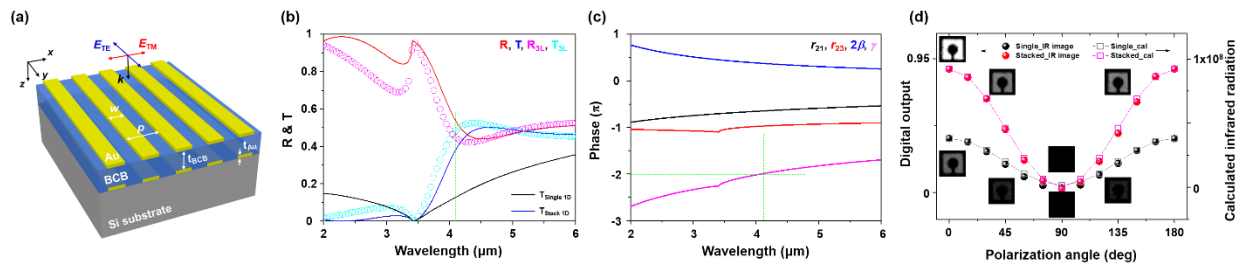


Figure 5 (a) Schematic of the stacked 1D gratings with geometric parameters. (b) The transmission and reflection (CST simulation and multiple-layer model). (c) The amplitude and phase terms in FP phase condition equation (r_{21} , r_{23} , 2β , γ). (d) T2SL based IR camera output and calculated IR intensity through fabricated samples.

C. High-performance polarizer using 1D gratings-dielectric structure Infrared polarimetric imaging has been widely used in remote sensing, military applications and environmental protection. 1-dimensional (1D) subwavelength grating integrated IR sensors have advantages such as polarization discrimination and a significant reduction in cost and complexity of IR camera systems. However, conventional 1D grating structures have low transmission efficiency for transverse magnetic (TM) polarized light due to unwanted reflections. Our design uses a 1D grating on top of the dielectric film, which can be integrated with a Type-II superlattice (T2SL) detector, thereby enabling enhanced responsivity for the TM polarization and thus giving rise to higher figure of merit (extinction ratio), as the measure of linear polarization detection performance than a conventional 1D grating. T2SL structures have been the focus of significant interest recently because of a high device-performance and bandgap engineering capabilities. In this study, we employed both the commercial software based on a finite integration technique and a rigorous coupled wave analysis for designing the structure of 1D grating atop the dielectric layer. Figure 6(a) shows

the calculated extinction ratio color map (1D grating on substrate) as a function of grating parameters (periodicity p and duty cycle r). The grating period p and the ratio r are varied continuously from 0.2 – 2.0 μm and 0 – 1 with fixed gold thickness at 100 nm. The extinction ratio (ER) at 4 μm is found to be from 1 - 10^5 for linear polarized light. The ER for the grating period $p = 0.4 \mu\text{m}$ and duty cycle $r = 0.7$ can reach up to $\sim 10^3$ while maintaining TM transmission higher than 50%. Next, we use SU-8 as the spacer between the 1D grating ($p = 0.4 \mu\text{m}$ and $r = 0.7$) and substrate. ER is represented in the color map as a function of wavelength and SU-8 dielectric thickness (t_{SU8} is varied from 0 to 2 μm with a step of 0.2 μm) as shown in Figure 6(b). In order to satisfy high TM transmission ($>70\%$) and ER ($>10^3$) simultaneously, an optimal SU-8 thickness was found to be $\sim 0.4 \mu\text{m}$. As indicated in Figure 6(a) and 6(b), the 1D grating on SU-8 spacer structures show overall performance enhancement (associated with linear polarization detection) as compared with a single layer 1D grating. Finally, the 1D grating and 1D grating-SU8 ($p = 0.4 \mu\text{m}$; $r = 0.7$; $t_{\text{SU8}} = 0.4 \mu\text{m}$) integrated backside-illumination T2SL detector (Figure 6(c)) were simulated for the overall polarization detection performance. Figure 6(d) indicates that TM absorption efficiency in 1D grating-SU8-T2SL can be improved up to $\sim 87\%$ as compared with 1D grating-T2SL and integration of extinction ratio ($\int ER(\lambda)d\lambda$) is also increased by \sim a factor of 10. We expect our design and analysis can be used for various IR polarimetric imaging applications.

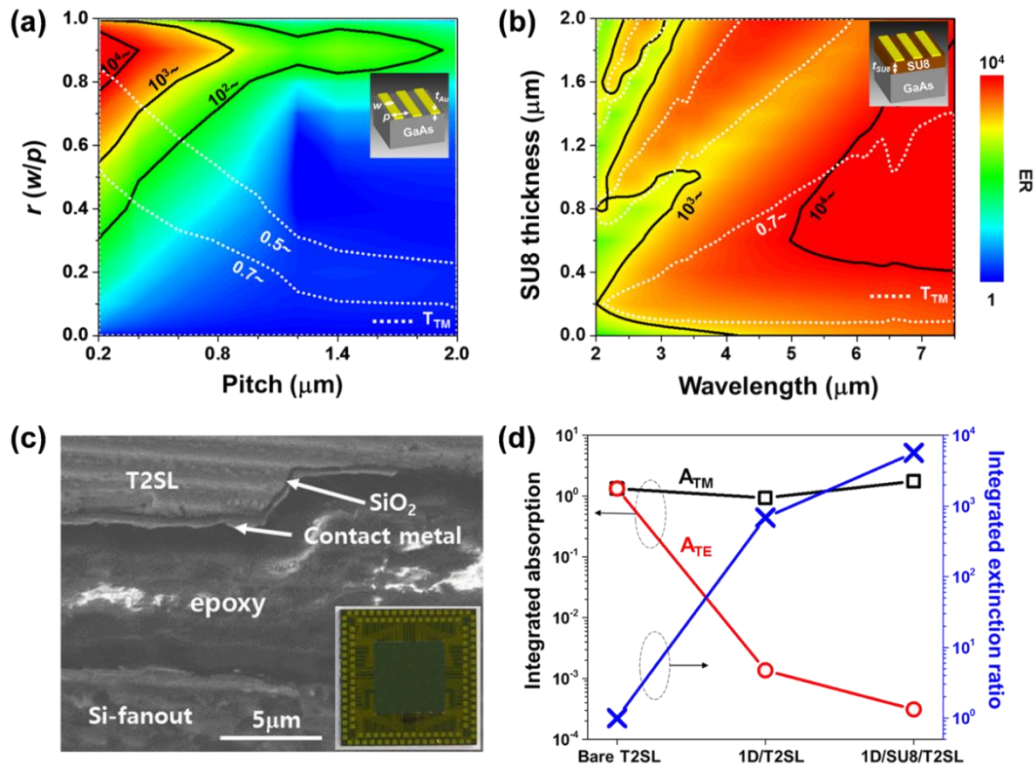


Figure 6. Extinction ratio color maps as a function of (a) p & r (1D grating) and (b) λ & t_{SU8} (1D grating-SU8). (c) Backside illumination T2SL detector. (d) Linear polarization detection performance of bare-T2SL, 1D grating-T2SL and 1D grating-SU8-T2SL detector: Integration of simulated absorption in the active layer for TM (black) and TE (red) modes and integration of ER (blue) with respect to the wavelength.

D. A surface plasmonic-cavity system We focused on analyzing the effect of a two-dimensional metal hole array structure and metal mirror back plane in a surface plasmonic-cavity system. Simulation results clearly show anti-crossing behavior resulting from interaction between the surface plasmon resonance and the Fabry-Perot resonance, depending on the thickness of the dielectric spacer. The simulation method provides a generalized approach to optimize the design of any type of couplers integrated with backside-illuminate infrared (IR) devices. In this work, we have investigated the resonances in the surface plasmon coupled cavity system. The system is composed of a dielectric spacer (benzocyclobutene: BCB) of variable thickness t_s (from 0.32 μm to 4.52 μm) sandwiched between a gold mirror back plane ($t_{\text{MGP}} = 0.2 \mu\text{m}$) and surface plasmon resonance structure (a gold film perforated with two-dimensional periodic array of subwavelength sized patterns: pitch $p = 3.2 \mu\text{m}$, diameter of circular aperture $d_m = 1.6 \mu\text{m}$, gold thickness $t_m = 0.05 \mu\text{m}$) as shown in Figure 7. Finite integration technique based simulations were carried out to study the physical origins of coupling between surface plasmon (SP) resonance and Farby-Perot (FP) resonance in the cavity. We gradually varied the BCB thickness t_s and numerically calculated the reflection of the SP-FP system. The spectral reflection colormap was used to show the spectral changes as shown in Figure 7. For $t_s = 0.32 \mu\text{m}$, zero reflection is achieved at 5.5 μm , which is the first order SP resonance. Higher order SP resonances can be found at shorter wavelengths. As t_s increases, the SP resonance is blue-shifted (up to the t_s of $\sim 1.72 \mu\text{m}$). At $t_s = 1.53 \mu\text{m}$, anti-crossing behavior is clearly observed due to two resonances, i.e., SP resonance and a half-wavelength ($\lambda/2$) FP mode. The simulated $\lambda/2$ FP mode shows good agreement with theoretically calculated FP mode (green dashed line) for the system bounded by two mirrors. Note that our SP-FP system is bounded by a mirror at one end and an SP structure at the other end, acting as the quasi-open boundary, thus giving rise to a small discrepancy between simulation and theory. Similar anti-crossing behavior can be also found between λ FP mode and 2nd order SP resonance at 3.12 μm . Understanding the underlying mechanism by means of a simulation may offer guidelines for the design of backside-illuminate IR detectors (including IR focal plane array) integrated with any type of resonators because these device structures (semiconductor and metal ground plane consisting of contact metals, under bump metallization, etc.) are similar to the system used here. We have tested various sets of geometric parameters ($t_s = 0.32, 1.21, 1.52, 1.7$ and $2.12 \mu\text{m}$ with fixed $p, d_m, t_m, t_{\text{MGP}}$ at 3.2, 1.6, 0.05, 0.2 μm , respectively) for experimental verification. Measured reflectance for $t_s = 2.12 \mu\text{m}$

shows good agreement with simulations for both transverse electric (TE) and transverse magnetic (TM) polarized incident IR.

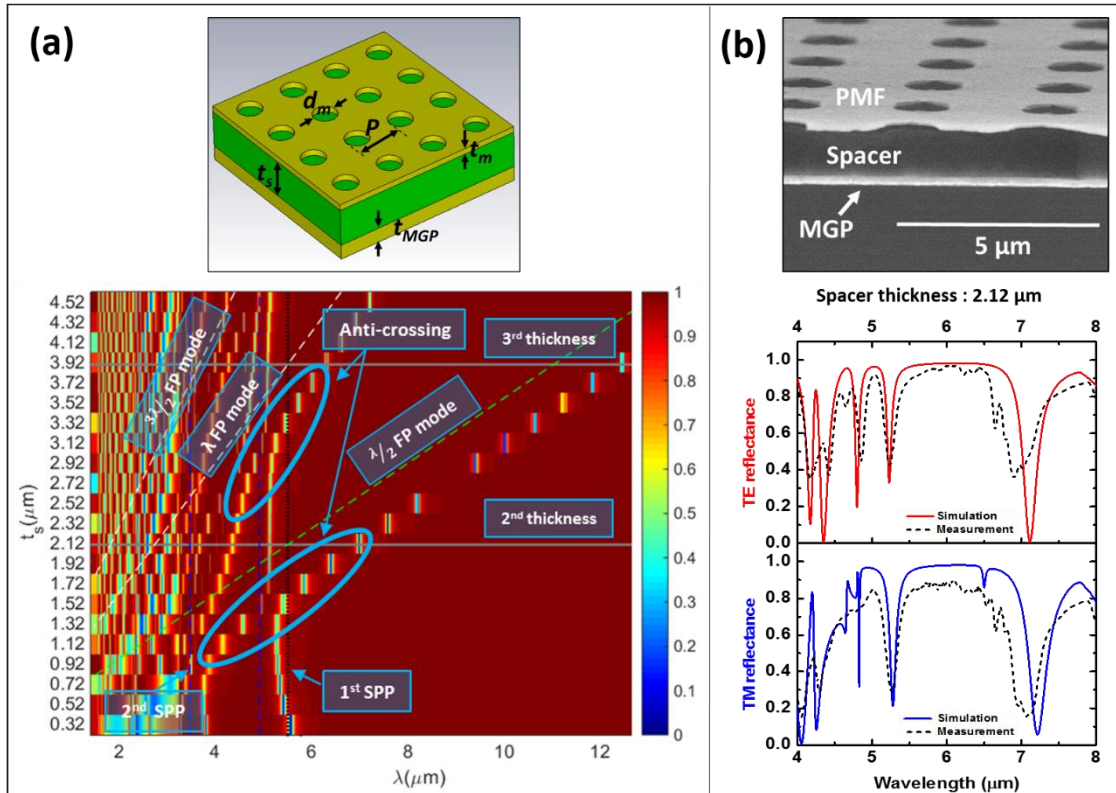


Figure 7. (a) Simulated reflection colormap for SP-FP system ($p = 3.2 \mu\text{m}$; $d_m = 1.6 \mu\text{m}$; $t_m = 0.05 \mu\text{m}$; $t_{MGP} = 0.2 \mu\text{m}$) as a function of the wavelength and BCB thickness t_s (varying from $0.32 \mu\text{m}$ to $4.52 \mu\text{m}$ with a step of $0.2 \mu\text{m}$). The unit cell of SP-FP system is illustrated in the upper panel. (b) Scanning electron microscope image of SP-FP system ($t_s = 2.12 \mu\text{m}$) and FTIR-measured reflectance for TE (red) / TM (blue) polarizations (solid and dashed lines represent the simulation and experiment, respectively).

E. Quasi-3D square coaxial aperture array

In recent years, the physical phenomenon of a metal hole grid structure has been demonstrated to have a high potential for use as multispectral sensing elements or couplers of infrared (IR) imagers. This surface plasmon (SP) resonance structure is suitable for integration with low performance IR detectors such as quantum dots and quantum well based detectors due to a sufficient coupling strength to active layer via local field engineering, thereby enabling spectral responsivity modifications to implement the IR retina concept (algorithmic spectrometry). In contrast, SP structure is inadequate to modify the spectral responsivity spectrum of type-II superlattice, InSb and MCT based detectors due to their strong light absorption of the active layer. For this reason, we focused our

attention on arrays of more complex unit cells offering additional degrees of freedom for controlling and optimizing the spectral responsivity of high performance IR detectors such as a subwavelength annular aperture (AA) array, first proposed by Baida. The use of such structure has several advantages over SP structure in terms of enhanced transmission compared with that through comparable diameter hole array, the ability to control the transmission peak wavelength and angular insensitive response. However, the fabrication of AA structure for the IR region of interest (3-12 μm) is required to use electron beam lithography or interference lithography in order to create the narrow gap in AA structure, which gives rise to a generally low throughput or complicated fabrication process, respectively. To get one step closer to useful application (i.e. the need of large-area patterning capability), we designed an alternative, easy-to-fabricate quasi 3-dimensional (3D) circular coaxial aperture (CCA) array, which is capable of adding a minimal amount of additional effort to conventional detector fabrication flows, more specifically, we used a process based on standard photolithography to fabricate a large-area, uniform, low-cost quasi 3D CCA array as illustrated in Figure 8.

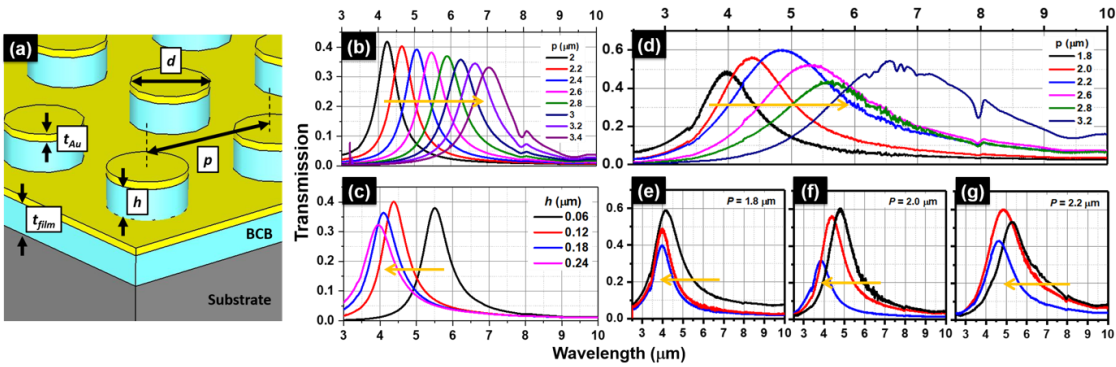


Figure 8. (a) Illustration of CCA. (b, c) FDTD-simulated and (d-g) FTIR-measured transmission of fabricated CCA samples with various pitches ranging from 2 to 3.4 μm (upper) and post-height (lower). The orange arrow indicates the peak shift as p and h are increased.